Additive-Manufactured Ordered Porous Structures Made of Ceria for Concentrating Solar Applications

Marie Hoes, Simon Ackermann, David Theiler, Philipp Furler, and Aldo Steinfeld*

Porous structures made of redox active ceria are attractive for high-temperature concentrating solar applications and particularly for the thermochemical splitting of H_2O and CO_2 as their enhanced heat and mass transport properties lead to fast reaction rates, especially with regard to the absorption of concentrated solar radiation during the endothermic reduction step. Hierarchically ordered porous structures, fabricated by the Schwartzwald replica method on 3D-printed polymer scaffolds, are experimentally assessed for their ability to volumetrically absorb high-flux irradiation of up to 670 suns. Temperature distributions across the porosity-gradient path are measured (peak 1724 K) and compared with that obtained for a reticulated porous ceramic (RPC) structure with a uniform porosity. To assist the analysis, a Monte Carlo ray-tracing model is developed for pore-level numerical simulations of the ordered geometries and applied to analyze the absorbing–emitting–scattering exchange and determine the radiation attenuation and the temperature distribution at a radiative equilibrium. In contrast to the Bouguer's law exponential-decay attenuation of incident radiation observed for the RPC, the ordered structures with a porosity gradient exhibit a step-wise radiative attenuation that leads to a more uniform temperature distribution across the structure. This in turn predicts a superior redox performance.

1. Introduction

The solar-driven splitting of H_2O and CO_2 via two-step thermochemical redox cycles has emerged as a thermodynamically favorable pathway to produce syngas—the precursor to liquid transportation fuels.[1,2] The state-of-the-art redox material for these cycles is nonstoichiometric ceria (CeO_2) because of its morphological stability and fast kinetics at high temperatures.[3–10] We have demonstrated the technical feasibility of the ceria-based redox cycle using a solar cavity receiver containing porous structures[11–15] and the entire production chain to solar kerosene

M. Hoes, Dr. S. Ackermann, D. Theiler, Dr. P. Furler, Prof. A. Steinfeld
Department of Mechanical and Process Engineering
ETH Zurich
8092 Zurich, Switzerland
E-mail: aldo.steinfeld@ethz.ch

The ORCID identification number(s) for the author(s) of this article can be found under https://doi.org/10.1002/ente.201900484.

from H_2O and CO_2.[16] It was shown that the morphology of the porous structure has a significant impact on the cycle's performance, e.g., on the molar conversion and energy efficiency, because the reduction step is heat transfer controlled, while the oxidation step is surface/mass transfer controlled.[13,17,18] Therefore, for a given volume of the solar cavity receiver, a desired porous structure should feature high mass loading for maximum fuel output, appropriate optical thickness for volumetric absorption and uniform heating during the endothermic reduction step, and a high specific surface area for rapid reaction kinetics during the exothermic oxidation step with H_2O and/or CO_2. Reticulated porous ceramic (RPC) foam-type structures with dual-scale interconnected porosity (mm- and μm-sized pores within the struts) fulfill some of these desired characteristics.[13] However, their uniform porosity and optical density results in Bouguer's law exponential-decay attenuation of incident radiation, which ultimately leads to an undesired temperature gradient along the radiation path over a wide range of structure morphologies (e.g., porosity).[19,20] This implies that parts of the RPC structure located far down the radiation path do not reach the desired reaction temperature (≈1773 K) and therefore are not utilized to their full potential.[21] In contrast, these parts become heat sinks without contributing to the solar-to-fuel conversion and thus detrimentally affect the energy efficiency. Radiative heat transport within the RPC can be calculated using its effective radiative properties, e.g., effective extinction coefficient and effective scattering phase function, which in turn can be computed via pore-level Monte Carlo (MC) simulation and other statistical approaches.[20,22–25] When the macro-porosity of the RPC is increased, its optical thickness decreases, radiation penetrates more deeply, which can improve the solar-to-fuel energy conversion efficiency to some extent,[26] provided the apparent density—defined as the ceria mass per unit volume of the porous structure—is not reduced. On the other hand, the maximum pore diameter and/or minimum strut thickness of the RPC fabricated by the replica method with polyurethane foams is limited due to its mechanical stability.[12,13]

Volumetric absorption of concentrated solar radiation using ceramic receivers has been intensively investigated.[27–29] Of special interest are structures featuring a porosity gradient obtained, e.g., by composites with different pore dimensions,[30]

by introducing spikes,[31] and more recently by hierarchically layered fractal-like structures.[32] The latter was fabricated by the additive manufacturing technique. Additive manufacturing offers the possibility of fabricating ordered porous structures with a tailored porosity gradient, with the goal of adjusting the optical thickness and achieving uniform heating without compromising the apparent density and/or the specific surface area.

This article describes the design and fabrication of four novel-ordered porous structures, made of ceria, and their experimental characterization when exposed to high-flux thermal radiation in ETH's high-flux solar simulator (HFSS). An MC ray-tracing simulation was performed to determine the radiative intensity attenuation and predict temperature distributions at radiative equilibrium. Numerically calculated temperatures were compared with the experimentally measured ones. Results of the ordered structures are compared with those obtained for a reference RPC structure with a uniform porosity, and the specific fuel output for each structure is predicted based on the calculated reduction extent at the measured temperature obtained for 360 suns irradiation.

2. Manufacturing and Modeling

2.1. Structure Fabrication

The ordered ceria structures were fabricated by the additive manufacturing method followed by the Schwartzwald replication method,[33] as schematically shown in **Figure 1**. In the first step, the hierarchically ordered geometries were designed with a commercial CAD software (Siemens NX 10.0). They consisted of uniform cells with a decreasing cell size in the direction of incident radiation, except the v-groove geometry that had a uniform porosity (**Table 1**). These geometries were 3D printed with a strut thickness of 0.3 mm. The resulting polymer templates were then coated with a ceria-based slurry that underwent sintering. Table 1 lists the characteristic of the reference RPC and the four ordered structures, namely, cube, pyramid, honeycomb, and v-groove. The pore sizes of the ordered structures varied from 9 mm at the front side to 3 mm at the rear side. The RPC structure with a uniform pore density, 10 ppi (pores per inch), was fabricated with similar dimensions and mass as a reference case for comparison. The mass of four fabricated samples per geometry varied within the range given in Table 1, and the arithmetic mean was used for further calculations. A scanning electron microscopy (SEM) image of the cross-section of a representative single strut of an ordered structure is shown in **Figure 2**. The μm-sized pores that result from the carbon fiber addition to the slurry are uniformly distributed within the strut. The hollow tube along the center line originates from the burning of the 3D-printed polymer template during sintering and exhibits less sharp edges compared with the RPC using polyurethane foam support. As the ordered and RPC structures were

manufactured by the same replica-based method, using the same ceria slurry, sintering protocol, and dimensions of the strut's inner hollow channel, the thermochemical stability of the ordered structures is expected to be comparable with that of the RPC structure subjected to the temperature-swing operating conditions of a solar reactor.[15] The cost of manufacturing was not assessed in this study.

2.2. Radiative Transport Model

The MC ray-tracing method using an in-house code (VeGaS+[34]) was applied for computing at the pore level the radiative attenuation and the temperature profile of the ordered structures for absorbing, emitting, and reflecting struts at a radiative equilibrium. **Figure 3** shows the scheme of the MC simulation of the HFSS setup and an example of the calculated temperature distribution across the pyramid structure. All surfaces were assumed opaque, diffuse, and gray, and the gas phase was assumed a nonparticipating medium. The geometric optics regime ($\frac{\pi \times d_{strut}}{\lambda} > 5$) was valid. The struts' surfaces were discretized as cylinders with a mesh element size of 0.25 mm. As the total hemispherical reflectivity of ceria ρ varies with the non-stoichiometry δ ($CeO_{2-\delta}$) and thus with temperature, it was calculated as a function of δ based on an empirical correlation,[35] whereas δ for a given p_{O_2} and T was calculated using a fit to the thermodynamic equilibrium data for pure ceria.[19,36] It was found that the variation of ρ within the investigated temperature range was negligible, and, thus, an average calculated value of $\rho = 0.45$ was used. The micro-scale porosity within the struts was omitted from consideration because of its negligible influence on the radiative exchange.[35] Representative volumes and planes of mirror symmetry (normal to the main direction of incoming radiation) were applied to save computational time. By treating the porous structures as participating media, the radiation penetration depth—defined as the mean path length to attenuation by absorption/scattering of incident radiation—is computed by pore-level MC assuming normal incident radiation and strut's blackbody surfaces (no reflections accounted). The temperature distribution was computed assuming a directional distribution of incident radiation given by the HFSS's characteristics and by considering multiple absorptions/reflections of incident and re-emitted radiation by the struts. The incident radiative flux was set to 360 kW m^{-2} to simulate the experimental conditions in the HFSS. Each ray was traced until it exited the cavity's control volume due to multiple reflections and/or re-emissions. Because energy is not accumulated within the struts, each absorbed ray was immediately re-emitted with the same radiative power. Temperatures were then determined at the end of the ray tracing based on the total absorbed flux on each surface element. Based on the results of an exemplary computational fluid dynamics (CFD) simulation (ANSYS 17.2) for the cube geometry, conductive and convective heat transports within
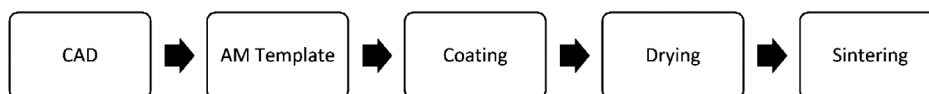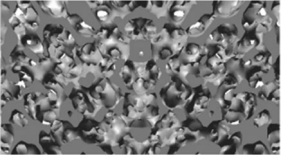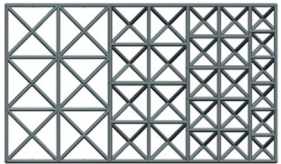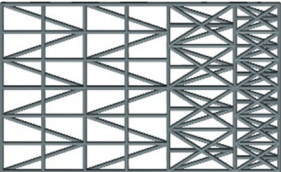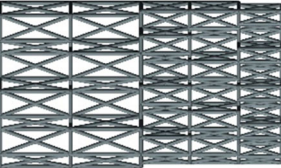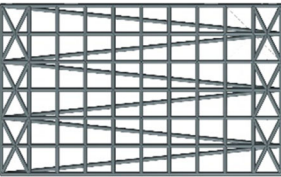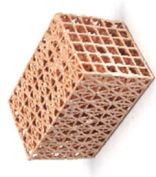

Figure 1. Manufacturing process chain of ordered ceria structures by the additive manufacturing and Schwartzwald replication methods.

Table 1. Photographs and morphological parameters of the ordered and RPC porous ceria structures.

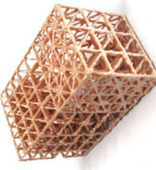| Name	RPC	Cube	Pyramid	Honeycomb	V-groove
CAD side view (incident radiation from top)					
Photograph after sintering					
Mass [g]	25.8–31.4	25.2–29.2	26.5–35.2	32.2–52.8	29.2–41.9
Dimensions [mm]	45 × 27 × 27	46 × 27 × 27	44 × 27 × 27	46 × 29 × 26	44 × 27 × 27
Apparent density [g cm^{-3}]	0.87	0.83	0.91	0.99	1.00
Specific surface area [mm^2 mm^{-3}] (excluding micro-scale pores)	1.2[19]	0.7	0.5	1.0	0.7

1900484 (3 of 8)

**ADVANCED
SCIENCE NEWS**

www.advancedsciencenews.com

Energy Technology
Generation, Conversion, Storage, Distribution
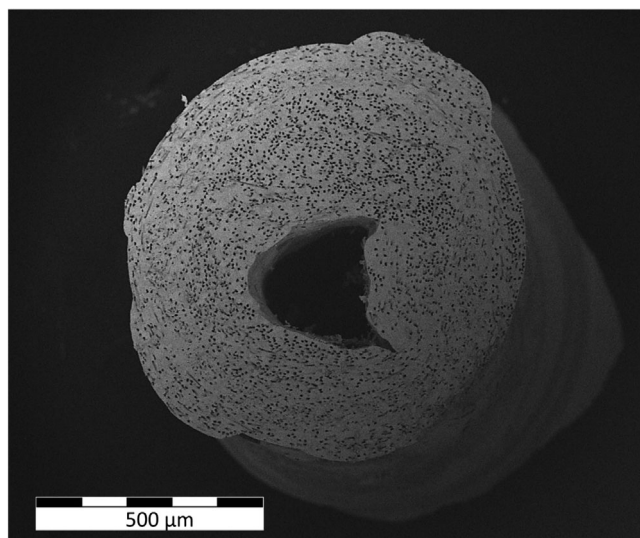
www.entechnol.de

Figure 2. A SEM image of the cross-section of a single ceria strut of an ordered structure. Pores in the micrometer range result from sacrificial carbon fibers that burned during sintering. The hollow channel stems from the burnt polymer scaffold.

the porous structure were found to be negligible when compared with the radiative transport and therefore omitted from consideration in the model. In the CFD simulation, the effective thermal conductivity and the convective heat flux were calculated for the relevant ranges of Re and Pr numbers. For a temperature drop across the structure not exceeding 600 K, the conductive heat flux represented less than 1.5% of the incoming radiative flux. For gas velocities not exceeding $0.02\,\mathrm{m\,s^{-1}}$ and the temperature difference between gas and solid phases not exceeding 900 K, the convective heat flux represented less than 0.5% of the incoming radiative flux. Heat losses through the cavity's Al_2O_3-SiO_2 insulation were implemented based on the steady-state conductive heat flow and unsteady sensible heat accumulation during heating, as the insulation required a longer time to reach steady state than the porous ceria structure. The higher thermal inertia of the insulation was also observed in previous solar experiments.[37] Simulations were performed with 1 million and 400 000 rays for the calculation of the

radiative penetration depth and temperature distributions, respectively. The mean standard deviation of the temperatures for three identical runs was less than 7 K. Convergence was verified with simulation runs with 4 million rays for all structures.

3. Results and Discussion

3.1. Attenuation

Figure 4 shows the numerically calculated attenuation of the radiative intensity as a function of the depth along the radiation path for parallel incident radiation perpendicular to the structure's front for the four ordered and the reference RPC structures (Table 1). As a result of the hierarchically ordered cell-based geometry, the radiation attenuation exhibits a step-wise profile that follows an approximately linear decay. In contrast, the radiation attenuation for the RPC exhibits a Bouguer's law profile that follows an exponential decay for a mean extinction coefficient of $498\,\mathrm{m^{-1}}$.[19] Clearly, the rate of attenuation is dictated by the gradient or a uniform porosity. The mean radiation penetration depths of the ordered structures are 17, 16, 13, and 11 mm for the honeycomb, pyramid, cube, and v-groove structures,
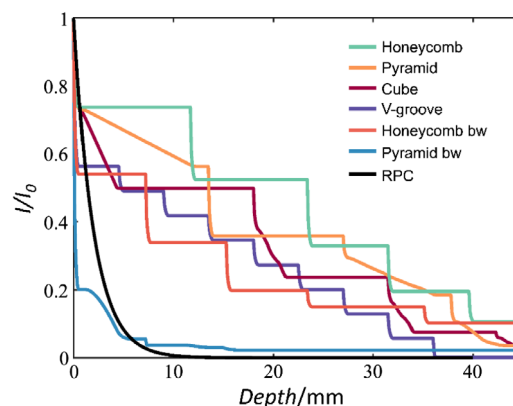

Figure 4. Numerically calculated attenuation of radiative intensity as a function of structure depth for parallel incident radiation for the four ordered and the reference RPC structures (Table 1). "bw" Denotes backward positioning.
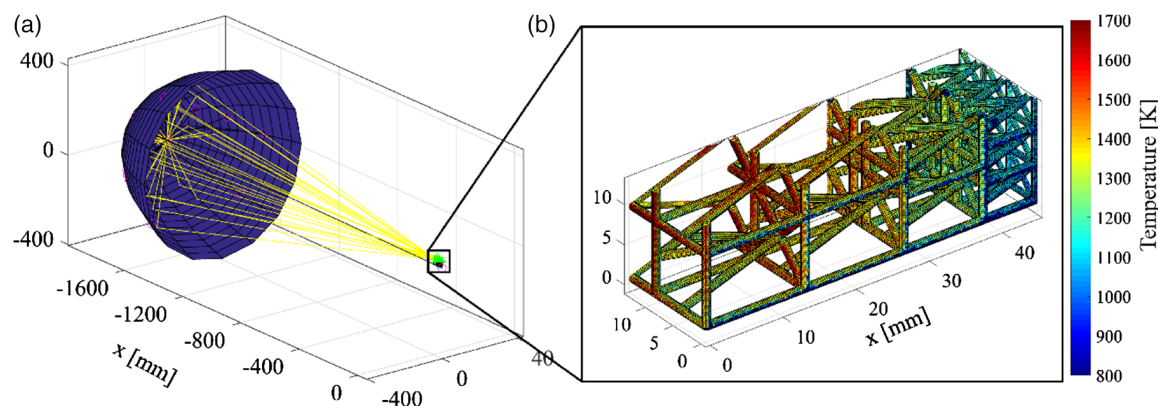

Figure 3. a) An MC ray-tracing method of the HFSS setup. b) Inset: calculated temperature distribution across the pyramid structure.

respectively. In comparison, the RPC exhibits a mean penetration depth of only 1.5 mm, indicating a much higher optical thickness. The front of the ordered structures is responsible for 26% attenuation in the honeycomb, pyramid, and cube, and 44% in the v-groove structure. In contrast, for the honeycomb and pyramid structures placed backward, 46% and 80% of incident radiation is attenuated by the front, respectively, yielding mean penetration depths of 7 and 1 mm, respectively. Obviously, a decreasing porosity in the radiation direction is preferred for volumetric absorption.

3.2. Heating Rate

The experimental setup is schematically shown in **Figure 5**. The structures were exposed for 1200 s to three constant mean radiative fluxes, namely, 120, 360, and 670 suns. **Figure 6** shows the measured temporal evolution of the temperatures at various depths for the honeycomb structure exposed to a mean incident radiative flux of 360 suns as well as for all tested structures exposed to a mean incident radiative flux of 670 suns. Approximate steady-state conditions (heating rate $< 10\,\text{K}\,\text{min}^{-1}$) were reached toward the end of the heating phase. As expected, the heating rate increases with the radiative flux leading to higher temperatures, whereas the relative temperature distribution along the depth is maintained. Maximum temperatures ($\approx$1724 K), heating rates, and radiative fluxes were comparable with the operating conditions of ceria-based solar reactors,[15] but in principle, required reduction temperatures can be reduced by applying vacuum pressures. The key boundary condition was the incident radiative flux. The RPC exhibits a large temperature drop between 10 and 20 mm depth due to its high optical thickness, yielding $\Delta T_{1-2,1200\,\text{s}} = 270\,\text{K}$ after 1200 s. This temperature difference is even more pronounced after 20 s yielding $\Delta T_{1-2,20\,\text{s}} = 570\,\text{K}$. In contrast, the ordered structures yielded a $\Delta T_{1-2,20\,\text{s}}$ of 270 K for the honeycomb, 143 K for the v-groove, 160 K for the pyramid, and 17 K for the cube, indicative of deeper penetration of incident radiation. The temperature difference between 10 and 40 mm depth is also smaller with $\Delta T_{1-4,20\,\text{s}} = 730\,\text{K}$ for the honeycomb, 715 K for the v-groove, 660 K for the pyramid, and 600 K for the cube when compared with 880 K for the RPC. However, the absolute temperature $T_{4,20\,\text{s}}$ was lower for the v-groove (640 K) than for the RPC (695 K), whereas it

was 820, 755, and 840 K for the honeycomb, pyramid, and cube, respectively. As the majority of the active mass is located at the rear side of the ordered structures, reaching the reaction temperature at this position is crucial. Additional experimental runs with thermocouples positioned at the center of the structure (14 mm from the side face) indicated a temperature that was, on average, 200 K higher than that measured 2 mm from the side face. As the structure was partially damaged by the deep insertion of the thermocouples, these measurements are not presented. Nevertheless, it is evident that the structures exhibited a temperature gradient normal to the direction of incident radiation, attributed to the heat loss through the Al_2O_3-SiO_2 insulation. Upon shut down of the HFSS, temperatures rapidly dropped and the front indicated the lowest temperature because of its larger re-radiation losses.

3.3. Temperature Distribution

Figure 7a shows the numerically calculated and experimentally measured temperatures as a function of depth at approximate steady-state conditions for the four ordered structures under a mean incident radiative flux of 360 suns. Calculated temperatures are area-averaged surface temperatures of neighboring struts ($\pm$3 mm in the main radiation x-direction, $\pm$4 mm in the z-direction, and 0–4 mm from the outside of the structure in the y-direction). The maximum relative difference between calculated and measured temperatures was within 7%. The discrepancy is partly due to uncertainties in the values assumed for the surface absorptivity and thermal conductivity of the Al_2O_3-SiO_2 insulation. All the ordered structures exhibited a smaller temperature gradient as compared with that for the RPC. The highest measured temperature of 1393, 1365, 1327, and 1318 K for the honeycomb, pyramid, cube, and v-groove structure, respectively, was reached at the second thermocouple positioned at 20 mm depth and not on the exposed front surface as it was the case with the RPC. This is attributed to an improved volumetric absorption due to higher radiative penetration depth and lower re-radiation losses at the front. The same trend was observed for solar receivers that feature a porosity gradient.[32] The lowest backside temperature was reached by the v-groove structure, partly because a large portion of the radiation (44%) is already attenuated at the front (Figure 5). The honeycomb structure performed the best: it reached the highest overall temperature with the lowest temperature gradient while having the highest mass of all structures. Figure 7b shows the measured temperature of the honeycomb and the pyramid structures when placed in default orientation and 180° rotated (backward). When placed backward, the honeycomb structure preserved an even temperature distribution since it possesses no diagonal struts and therefore maintained a linear radiation attenuation. In contrast, the pyramid structure performed poorly when placed backward because of the higher reflection and re-radiation losses.

3.4. Redox Performance

The oxygen release during the reduction step is indicative of the fuel (H_2, CO) production during the oxidation step. It was shown in solar reactor experiments that ceria reduction proceeds at fast rates and closely approaches thermodynamic equilibrium.[12]

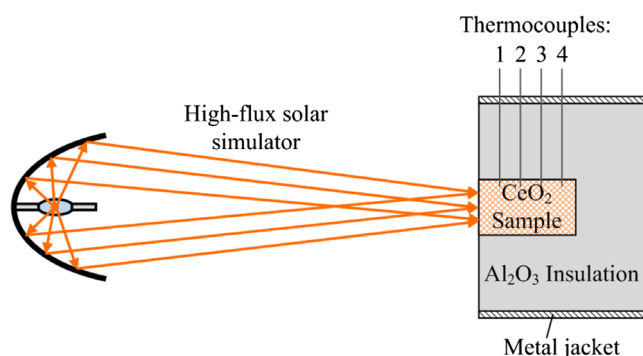

Figure 5. Schematic of the experimental setup. The sample temperature is measured at four positions: 10, 20, 30, and 40 mm from the frontal face along the direction of incident radiation and 2 mm from the side face.
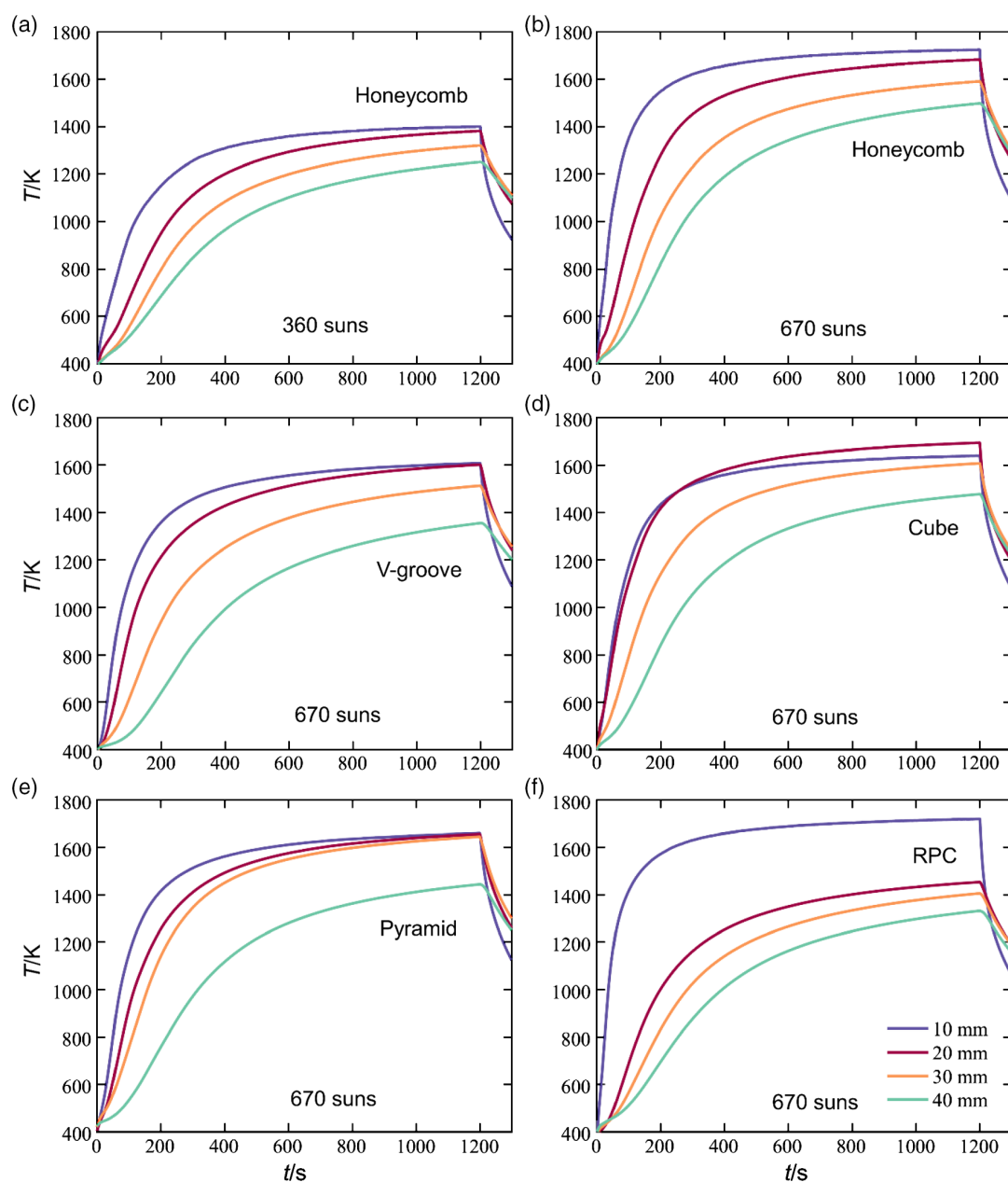
Figure 6. Measured temporal evolution of temperatures along the direction of incident radiation at a depth of 10, 20, 30, and 40 mm for: a) the honeycomb structure exposed to 360 suns, and b) the honeycomb, c) the v-groove, d) the cube, e) the pyramid, and f) the RPC structures, all exposed to 670 suns.

Thus, the specific oxygen release was calculated assuming a thermodynamic equilibrium at the measured temperature and given O_2 partial pressure. **Table 2** shows the calculated specific oxygen release per mass of ceria for the four ordered and RPC structures based on the measured temperatures for 360 suns after 1200 s (Figure 7a) and the calculated reduction extent. δ was determined by integrating over 1 mm slices and using a fit to the thermodynamic equilibrium data for pure ceria[19,36] at the measured steady-state temperature and under typical reduction conditions of $p_{O2} = 1 \times 10^{-4}$ atm. All ordered structures reach a higher specific oxygen release than the RPC, with the honeycomb structure

releasing the most and more than three times that of the RPC (4.03×10^{-5} and 1.20×10^{-5} g g_{ceria}^{-1}, respectively). This is mainly a consequence of the higher heating rate and more uniform temperature distributions for the ordered structures while having approximately the same mass and volume per tested sample.

4. Summary and Conclusion

We have designed, fabricated, and characterized four hierarchically ordered porous ceria structures for solar thermochemical redox
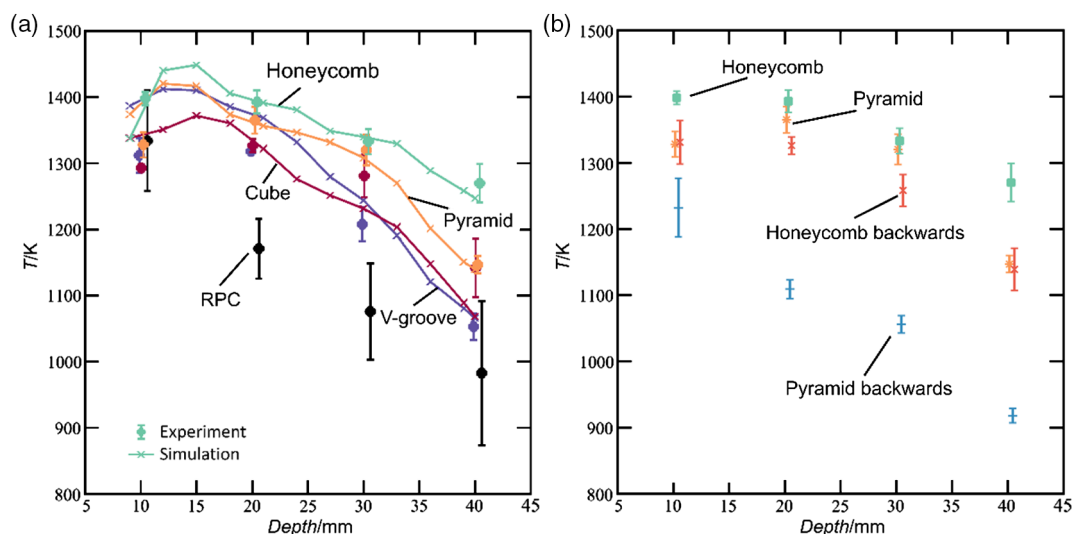
ADVANCED
SCIENCE NEWS

www.advancedsciencenews.com

Energy Technology
Generation, Conversion, Storage, Distribution

www.entechnol.de

Figure 7. a) Numerically calculated and experimentally measured steady-state temperatures of the four ordered structures (Table 1) as a function of depth for an incident mean flux of 360 suns. Included is the measured temperature distribution for the reference RPC. b) Comparison between the experimentally measured temperatures of the honeycomb and pyramid structures when placed forward and backward in the cavity.

Table 2. Calculated oxygen release of the four ordered and the reference RPC structures (Table 1) at the measured steady-state temperature distribution (Figure 7a) and $p_{O_2} = 1 \times 10^{-4}$ atm.

Structure	RPC	V-groove	Cube	Pyramid	Honeycomb
Oxygen release [g g_{ceria}^{-1}]	1.20E-05	1.59E-05	1.35E-05	2.31E-05	4.03E-05

splitting of H_2O and CO_2. The structures' green bodies were fabricated by additive manufacturing and coated with ceria according to the Schwartzwald replication method. The fabrication method proved to be successful with a 100% survival rate of all manufactured samples after sintering. All ordered structures with a porosity gradient exhibited a higher radiation penetration depth than the reference RPC with a uniform porosity, leading to a more uniform temperature distribution, as indicated by Monte-Carlo ray-tracing simulations and corroborated experimentally. Numerically calculated and experimentally measured temperatures matched within 7%. Furthermore, compared with the RPC, the ordered structures exhibited higher heating rates and reached peak temperatures within the volume and not on the exposed frontal surface, which is attributed to improved volumetric radiative absorption and is leading to superior calculated redox performance.

5. Experimental Section

Materials: Polymer scaffolds of the ordered structures were fabricated by the multijet modeling method (3D-Labs GMBH) using an acrylic plastic (Visijet EX200) as the carrier material. The scaffolds were coated with a ceria-based slurry consisting of cerium (IV) oxide powder (Sigma Aldrich, $d < 5\,\mu m$, purity 99.9%), deionized water, deflocculant agent (Dolapix CE 64), and binder (Optapix PA 4G). In addition, 30 vol% carbon fibers (Sigrafil) were included in the slurry for micro-scale porosity formation within the struts. The coated templates were finally sintered at 1873 K, which burned the polymer scaffolds and the carbon pore former.

Outer dimensions of all the samples after sintering were approximately $27 \times 27 \times 45$ mm with 1 mm struts.

Analysis: SEM was performed on a Hitachi TM-1000, with 15 kV accelerating voltage.

Experimentation: The ETH's high-flux solar simulator comprised an array of high-pressure Xenon arcs, each closed-coupled with truncated ellipsoidal specular reflectors, for providing a source of intense thermal radiation—mostly in the visible and IR spectra—that closely approximated the heat-transfer characteristics of highly concentrating solar systems. The radiative flux distribution at the sample front was measured optically using a charge couple device (CCD) camera focused on a Lambertian (diffusely reflecting) target and calibrated with a thermal flux gage (Sequoia Technology). The samples were placed inside a cavity made of Al_2O_3–SiO_2 insulating material (UltraBoard, Schupp) and were directly exposed to a solar concentration ratio of up to 670 suns (1 sun equivalent to 1 kW m^{-2}) to mimic realistic operating conditions inside a cavity-type solar reactor containing the porous ceria structures. In solar reactors, peak solar concentration ratios exceeding 5000 suns were achieved at the cavity's aperture, but those incident on the surface of the porous structures are typically an order of magnitude lower as the solar concentrated radiation entering the cavity diverges. The temperature distribution was measured with four B-type thermocouples, which were coated with ceria to ensure comparable radiative properties and placed inside the structure (approximately 2 mm from the side face) along the radiation direction (10, 20, 30, and 40 mm). Experiments were performed under air at atmospheric pressure.

Acknowledgements

Conflict of Interest

The authors declare no conflict of interest.

[1] C. L. Muhich, B. D. Ehrhart, I. Al-Shankiti, B. J. Ward, C. B. Musgrave, A. W. Weimer, *Wiley Interdiscip. Rev.: Energy Environ.* **2016**, *5*, 261.

[2] M. Romero, A. Steinfeld, *Energy Environ. Sci.* **2012**, *5*, 9234.

[3] S. Abanades, G. Flamant, *Sol. Energy* **2006**, *80*, 1611.

[4] S. Ackermann, J. R. Scheffe, A. Steinfeld, *J. Phys. Chem. C* **2014**, *118*, 5216.

[5] W. C. Chueh, S. M. Haile, *ChemSusChem* **2009**, *2*, 735.

[6] X. Gao, A. Vidal, A. Bayon, R. Bader, J. Hinkley, W. Lipinski, A. Tricoli, *J. Mater. Chem. A* **2016**, *4*, 9614.

[7] N. Gokon, S. Sagawa, T. Kodama, *Int. J. Hydrogen Energy* **2013**, *38*, 14402.

[8] N. Knoblauch, L. Dorrer, P. Fielitz, M. Schmucker, G. Borchardt, *Phys. Chem. Chem. Phys.* **2015**, *17*, 5849.

[9] J. R. Scheffe, A. Steinfeld, *Mater. Today* **2014**, *17*, 341.

[10] A. C. Gladen, J. H. Davidson, *Sol. Energy* **2016**, *139*, 524.

[11] W. C. Chueh, C. Falter, M. Abbott, D. Scipio, P. Furler, S. M. Haile, A. Steinfeld, *Science* **2010**, *330*, 1797.

[12] P. Furler, J. Scheffe, M. Gorbar, L. Moes, U. Vogt, A. Steinfeld, *Energy Fuels* **2012**, *26*, 7051.

[13] P. Furler, J. Scheffe, D. Marxer, M. Gorbar, A. Bonk, U. Vogt, A. Steinfeld, *Phys. Chem. Chem. Phys.* **2014**, *16*, 10503.

[14] P. Furler, J. R. Scheffe, A. Steinfeld, *Energy Environ. Sci.* **2012**, *5*, 6098.

[15] D. Marxer, P. Furler, M. Takacs, A. Steinfeld, *Energy Environ. Sci.* **2017**, *10*, 1142.

[16] D. Marxer, P. Furler, J. Scheffe, H. Geerlings, C. Falter, V. Batteiger, A. Sizmann, A. Steinfeld, *Energy Fuels* **2015**, *29*, 3241.

[17] L. J. Venstrom, N. Petkovich, S. Rudisill, A. Stein, J. H. Davidson, *J. Sol. Energy Eng.* **2011**, *134*, 11005.

[18] C. D. Malonzo, R. M. De Smith, S. G. Rudisill, N. D. Petkovich, J. H. Davidson, A. Stein, *J. Phys. Chem. C* **2014**, *118*, 26172.

[19] S. Ackermann, M. Takacs, J. Scheffe, A. Steinfeld, *Int. J. Heat Mass Transfer* **2017**, *107*, 439.

[20] D. J. Keene, J. H. Davidson, W. Lipiński, *J. Heat Transfer* **2013**, *135*, 052701.

[21] D. J. Keene, W. Lipiński, J. H. Davidson, *Chem. Eng. Sci.* **2014**, *111*, 231.

[22] A. V. Gusarov, *J. Heat Transfer* **2018**, *140*, 112701.

[23] A. V. Gusarov, *J. Heat Transfer* **2018**, *141*, 012701.

[24] S. Haussener, P. Coray, W. Lipiński, P. Wyss, A. Steinfeld, *J. Heat Transfer* **2009**, *132*, 023305.

[25] J. Petrasch, P. Wyss, A. Steinfeld, *J. Quant. Spectrosc. Radiat. Transfer* **2007**, *105*, 180.

[26] S. Zoller, E. Koepf, P. Roos, A. Steinfeld, *J. Sol. Energy Eng.* **2019**, *141*, 021011.

[27] C. C. Agrafiotis, I. Mavroidis, A. G. Konstandopoulos, B. Hoffschmidt, P. Stobbe, M. Romero, V. Fernandez-Quero, *Sol. Energy Mater. Sol. Cells* **2007**, *91*, 474.

[28] A. L. Ávila-Marín, *Sol. Energy* **2011**, *85*, 891.

[29] B. Hoffschmidt, V. Fernández, A. G. Konstandopoulos, I. Mavroidis, M. Romero, P. Stobbe, F. Téllez, in *5th Cologne Solar Symposium*, DLR, Cologne, Germany **2001**, pp. 51–61.

[30] X. Chen, X.-L. Xia, X.-W. Yan, C. Sun, *Energy Convers. Manage.* **2017**, *136*, 262.

[31] R. Capuano, T. Fend, H. Stadler, B. Hoffschmidt, R. Pitz-Paal, *Renewable Energy* **2017**, *114*, 556.

[32] S. Luque, G. Menéndez, M. Roccabruna, J. González-Aguilar, L. Crema, M. Romero, *Sol. Energy* **2018**, *174*, 342.

[33] K. Schwartzwalder, A. V. Somers, Google Patents, **1963**.

[34] J. Petrasch, in *ASME 2010 4th Int. Conf. on Energy Sustainability*, Vol. 2, Phoenix, USA **2010**, pp. 125–132.

[35] S. Ackermann, A. Steinfeld, *Sol. Energy Mater. Sol. Cells* **2017**, *159*, 167.

[36] R. J. Panlener, R. N. Blumenthal, J. E. Garnier, *J. Phys. Chem. Solids* **1975**, *36*, 1213.

[37] P. Furler, A. Steinfeld, *Chem. Eng. Sci.* **2015**, *137*, 373.